Synthetic Control and Bioconjugation of Magnetite Nanoparticles for the Development of an *in vivo* Glucose Sensor

By
Phillip W. Gingrich

Submitted to the graduate degree program in Chemistry and the Graduate Faculty of the University of Kansas in partial fulfillment of the requirements for the degree of Master of Science.

_____

Shenqiang Ren, PhD, Assistant Professor (Chair)

_____

Mark Richter, PhD, Professor

_____

Cindy L. Berrie, PhD, Associate Professor

Date Defended: 15 July 2014

The Thesis Committee for Phillip W. Gingrich

certifies that this is the approved version of the following thesis:

Synthetic Control and Bioconjugation of Magnetite Nanoparticles for the Development of an *in vivo* Glucose Sensor

_____

Shenqiang Ren, PhD, Assistant Professor (Chair)

_____

Mark Richter, PhD, Professor

_____

Cindy L. Berrie, PhD, Associate Professor

Date approved: 7-15-14

Abstract

In this work, an examination into the synthesis, functionalization, and utility of iron oxide nanoparticles was conducted for the development of an in vivo glucose biosensor based on the catalytic cycle of glucose oxidase and amperometric detection of hydrogen peroxide. While enzyme conjugation to a nanoparticle has been reported in the literature, this study focuses on the role of the nanoparticles as electrophoretic charge carriers for sensor fabrication.

The kinetically controlled growth of magnetite (Fe_3O_4) nanoparticles was investigated utilizing the thermal decomposition method and iron (III) stearate as a readily available and economical precursor. Nucleation periods were observed to be kinetically controlled by and directly proportional to the surfactant concentration, giving a linear relationship between the surfactant concentration and particle diameters below 20 nm. Narrow size distributions were achieved, with standard deviations of particle populations being 2-4 nm. A precise empirical growth model was determined for low surfactant concentrations.

As synthesized Fe_3O_4 nanoparticles presented a hydrophobic surface with no appreciable surface charge as determined by electrophoretic light scattering. Surface functionalization was attempted via base catalyzed condensation of (3-aminopropyl)trimethoxysilane, followed by nucleophilic ring opening of two cyclic anhydrides, yielding an aqueous suspension of particles with ζ potentials of approximately -50 mV. Enzyme-particle conjugation was done via known carbodiimide/N-hydroxyl succinimide chemistry. The resulting bioconjugates were electrodeposited onto glass/platinum capillary electrodes, and glucose response was measured. Sub-optimal responses were realized, owing to aggregation of particle cores prior to functionalization as observed by dynamic light scattering. The same aggregation was not observed by transmission electron microscopy.

Acknowledgements

First and foremost, I would like to thank my wife and family for the love and support they have extended to me during this work. Their encouragement and patience has been paramount in the completion of my studies.

To my advisor, Dr. Shenqiang Ren, I am thankful for his direction on this project, opportunities to assist on other projects with the group where I could, and being supportive of my many endeavors, academic, personal, and professional alike.

To our collaborators on this work, specifically Dr. George Wilson, Dr. Mark Richter, Dr. Peter Petillo, Dwight Deay, and Donald Gwartney, thank you for your energy and commitment to this project. It has truly been a team effort to understand the complexity of this project.

To my fellow graduate students in the Ren Research Group, thank you for the multiple discussions, academic and otherwise, that helped me to see ways ahead on this project and for giving me the opportunity to contribute in whatever ways I could to your works. I wish you all the best in the rest of your graduate studies and careers afterwards.

To the staff of the Microscopy and Analytical Imaging Laboratory, particularly Dr. David Moore and Heather Shinogle, thank you for the training and assistance with the electron microscopes and image analysis. These skills have proven invaluable.

Lastly, I would like to thank the rest of the faculty and staff of the KU Chemistry Department for challenging me, both in class and with teaching assignments outside of my research interests. My graduate studies have been fulfilling because of your commitment.

Table of Contents

List of Figures

List of Tables

List of Equations

1. Introduction

1.1. Goals

The overarching goal of this work is to develop a biological sensor for *in vivo* monitoring of glucose utilizing electrochemical means of detection, specifically the amperometric analysis of the enzymatic conversion of glucose and molecular oxygen to the resultant lactone and, more importantly for detection, hydrogen peroxide by glucose oxidase. The biosensors will be based on small, micron-sized capillary-type electrodes that require the use of electrodeposition to evenly deposit the active enzyme layer. Electrodeposition is required due to this spatial confinement. However, electrodeposition of unfunctionalized glucose oxidase is inefficient because the enzyme is weakly charged, so it will become necessary to conjugate the enzyme and a charge-carrier. Here, surface-functionalized nanoparticles will be used in order to improve the electrophoretic mobility of the overall nanoparticle-enzyme bioconjugate. While improved sensor response could be realized through examining the activity of deposited enzyme and working to optimize that activity, the goal of this work is to initially focus on the deposition of bioconjugates.

1.2. Electrophoresis and Electrodeposition

In order to motivate this work, it is appropriate at this point to briefly discuss some introductory theory behind electrophoresis. In doing so, the necessary physical parameters of a nanoparticle-enzyme bioconjugate will be established to guide the rational design of such a bioconjugate for the successful employment of electrodeposition in the fabrication of a biological sensor.

Electrodeposition occurs via electrophoresis. The movement of charged species occurs within an applied electric field, and the achievement of deposition can be understood within that

context. As in capillary electrophoresis (CE), the separation of analytes occurs according to their electrophoretic mobility. The electrophoretic mobility, μ, of a species in solution under an applied potential is proportional to the charge of the species, q, and inversely proportional to the translational friction coefficient, f. For spherical particles, that coefficient of friction is equal to $3\pi\eta d$, where η is the viscosity of the run buffer and d is the particle diameter.[1]

$$\mu = \frac{\mu_q}{q} = \frac{1}{f} = \frac{1}{3\pi\eta d}$$

Equation 1.1 Electrophoretic mobility of a charged spherical particle

A neutral analyte will not migrate as a result of the interaction between itself and the field, and oppositely charged analytes migrate in the opposite direction within the applied electric field. Thus, the applied bias dictates the order in which species will be detected on the basis of charge. However, all species, albeit at different rates, can migrate over time with the electroosmotic flow that results from the motion of all the ions within the capillary. In fact, deposition of non- or weakly charged species can be and often is done in an excess of supporting electrolyte, in which case mobility is due to the electroosmotic flow and a concentration gradient is the driving force for deposition, as has been shown specifically in the case of glucose oxidase.[2] While this work is not concerned with the conduct of an analytical separation by CE, it suffices to conclude from this that the presence of sufficient charge is helpful for the efficient movement of species within the field. Once a species has reached the electrode surface, deposition occurs and van der Waals forces retain the material in place.

For the purpose of this project, the efficient deposition of glucose oxidase onto an electrode surface is critical to the sensitivity and shelf-stability of the sensor. However, it has been shown that glucose oxidase has an isoelectric point of 4.2 and carries little negative charge at biologically relevant pH.[3] This is attributed to only 69 acidic amino acid residues in the 583

residue primary structure of the enzyme, all of which are not located on the folded enzyme's surface and are sterically unavailable for covalent attachment or surface charge generation.[4] As a result, this renders the electrodeposition of glucose oxidase alone inefficient, so a charge-carrier must be introduced to carry the enzyme to the electrode surface during deposition. Covalently attaching glucose oxidase to a nanoparticle whose surface has been functionalized to present a negative charge will provide the necessary electrophoretic mobility to achieve deposition.

As previously stated, the electrophoretic mobility is reduced by an increase in the size of the species. While such a nanoparticle-enzyme bioconjugate will certainly not be spherical, the physical trend is apparent from this simplification that an increase in size of a species from the molecular scale to the 10-1000 nm scale will decrease the electrodeposition efficiency. However, electrodeposition has been shown as a useful technique for the creation of ordered nanostructures on electrode surfaces, both as a synthetic technique generating zero-valent metal nanostructures[5] and for deposition of preformed gold nanoparticles as a chitosan-glucose oxidase biocomposite.[6] Electrodeposition of nanostructures has also found use in solar cell fabrication with nanocrystalline films of TiO_2 at low electric potentials, and film thickness in this system was shown to be dependent on the deposition time.[7] Building from these investigations, this work will employ electrodeposition of a bioconjugate of glucose oxidase with a nanoparticle charge-carrier, specifically iron oxide (magnetite, Fe_3O_4), to fabricate a glucose biosensor with the goal of *in vivo* amperometric determination of glucose.

2. Kinetic Control of Magnetite Nanoparticle Size

2.1. Introduction

Colloidal iron oxide, specifically magnetite (Fe_3O_4) has found considerable use for biological applications; superparamagnetic iron oxide nanoparticles (IONPs) are of widespread interest for protein isolation,[8] targeted chemotherapy drug delivery,[9] MRI imaging,[10] and hyperthermia-induced tumor necrosis.[11] The commercialization of IONP-based assays and treatments will require synthetic reproducibility through an understanding of the effects of reaction conditions. According to LaMer's classical crystal growth mechanism (Figure 2.1), nucleation occurs once monomer concentration has reached a critical threshold, and growth occurs on existing nuclei by diffusion.[12]

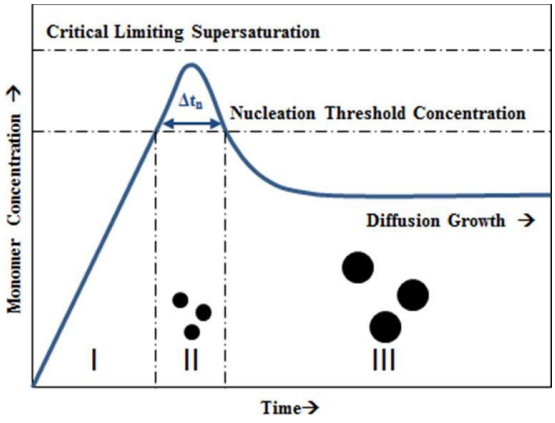

Figure 2.1 LaMer's Classical Nucleation and Growth Model[12-13]

Ostwald Ripening, or some other aggregative or coalescent growth mechanism, can take place with thermal annealing following nucleation. These concepts have been recently reviewed by Buhro et al.[13] Additionally, economic considerations for up-scaling need attention, particularly when choosing a precursor. The co-precipitation method, perhaps the most classical method for the synthesis of colloidal iron oxide, utilizes stoichiometric amounts of ferrous and ferric salts in basic media; however, polydisperse samples are the typical result.[10] Sun et al. have

demonstrated a seeded growth route to grow larger crystals with sequential additions of starting materials; while more laborious than other methods, this approach yields monodisperse populations of IONPs.[14] Alivasatos et al. have monitored the temporal size evolution of synthesizing iron oxide from iron pentacarbonyl; while easily manipulated using standard air-free techniques, metal carbonyls present a health hazard and should be avoided where possible.[15] Most promisingly, Peng et al. reported on the thermal decomposition of organometallic iron precursors, specifically iron (III) oleate; as presented, the method is also laborious by requiring the synthesis and concentration determination of the organometallic iron precursor.[16] What is required is a safe, simple method for the synthesis of monodisperse IONPs that demonstrates consistent and predictable control over particle size.

In this work, the effects of surfactant concentration on particle diameter were examined using a non-toxic, economically available precursor. The resultant particle distributions were analyzed, yielding a linear relationship between ligand concentration and the average particle diameter, as well as the duration of the nucleation period. Ostwald Ripening, which predicts a linear growth in the cubed mean radius of the particle population, is not observed over the annealing time for this system, but an alternative empirical model is proposed. This thermal decomposition method shows simplicity and viability for up-scaling.

2.2. Materials and Methods

2.2.1. Materials.

Iron (III) stearate was procured from TCI America. Oleic acid and 1-octadecene were procured from Sigma-Aldrich. Wash solvents (hexane, isopropyl alcohol, and acetone) were laboratory grade from varying sources. All materials were used as received without further purification.

2.2.2. Transmission Electron Microscopy and Image Analysis

Transmission Electron Microscopy (TEM) was conducted on an FEI Tecnai F20 XT Field Emission Transmission Electron Microscope operated at 200kV. Samples were prepared by drop-casting dilute solutions on to amorphous carbon-coated copper TEM grids. ImageJ version 1.47 was used to analyze particle size distributions obtained from TEM images. Briefly, a Gaussian Blur was applied with a sigma value of 2 pixels. Background was subtracted utilizing the rolling ball method with a radius of 50-80 pixels (depending on image scale). In all cases, the signal threshold was set utilizing the Otsu watershed method.[17] Particles were limited to a minimum circularity of 0.7 to 0.8 and a minimum area of π nm^2, which effectively eliminated any background speckling and overlapped/stacked particles. Particles were modelled spherically, and the diameter of each particle was calculated as the average from both the perimeter and area, with the standard deviation also calculated from this quantity.

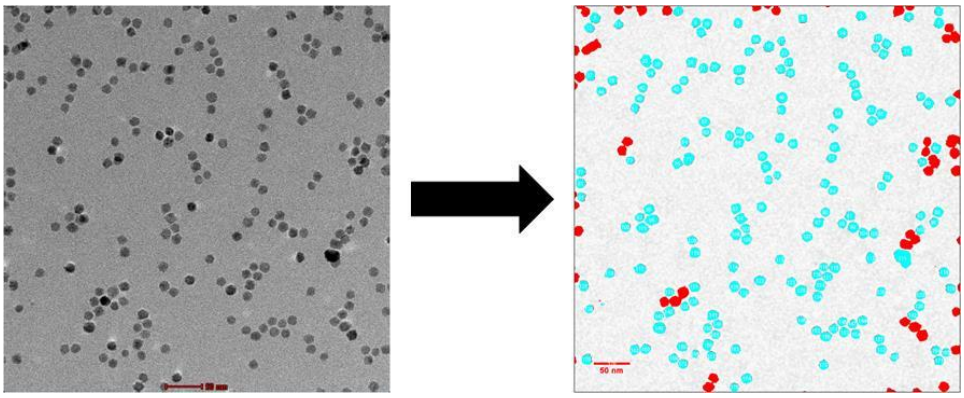

Figure 2.2 Example resultant image following analysis by ImageJ, were red particles have been excluded and light blue particles were utilized for core diameter measurements

Figure 2.2 Figure 2.1provides an example of the image analysis conducted. Light blue particles are those whose areas and circumferences were measured and included in statistical analysis, while red particles did not meet the requirements listed above (due to particle stacking, touching, etc.) as the measurements would skew the average due to being treated as one particle instead of independent particles.

2.2.3. Synthesis of Iron Oxide Nanoparticles.

This method was adapted from elsewhere in the literature.[16] As an example, a reaction mixture of 0.5044g (56.4 mmolal) iron (III) stearate and 700 μL (223 mmolal) oleic acid was made up in 12500 μL of 1-octadecene and placed under a blanket of Ar with a magnetic stir bar, an analog 400°C mercury thermometer, and a water-cooled condenser in a 50 mL three-neck flask. The reaction mixture was wrapped in aluminum foil and rapidly heated to the reflux temperature of 321°C. The orange mixture gave way to a deep red solution, followed by a translucent tan-colored solution, and finally a black suspension of particles was achieved. The suspension was allowed to anneal at the reflux temperature for one hour.

Once cooled to room temperature, particles were washed three times with hexane and isopropyl alcohol or acetone with centrifugation, isolating a black pellet after each wash and discarding the supernatant. After washing, the pellet was suspended in hexane, and a dilute sample was prepared for analysis by TEM.

To confirm the phase of iron oxide synthesized, room temperature X-ray powder patterns were obtained using monochromated Cu-Kα radiation ($\lambda = 1.54178$ Å) on a Bruker proteum diffraction system equipped with Helios multilayer optics, an APEX II CCD detector and a Bruker MicroStar microfocus rotating anode X-ray source operating at 45 kV and 60 mA. The powders were mixed with a small amount of Paratone N oil to form a paste that was then placed in a small (<0.5 mm) nylon cryoloop and mounted on a goniometer head.

2.2.4. Kinetic Measurements.

For kinetic measurements, the timer was started as soon as the magnetic stir bar was visually distinguishable within the solution. The timer was stopped once an opaque black

suspension of IONPs was generated. The visually observed time was taken as proportional to the true nucleation window time (specifically, $\Delta \dot{t}_n \approx c\Delta t_n$, where Δt_n is defined below).

2.3. Results and Discussion

2.3.1. Nanoparticle Synthesis by Thermal Decomposition.

Previously reported thermal decomposition methods for the synthesis of magnetite have commonly utilized iron (III) oleate as the organometallic precursor, first synthesizing iron (III) oleate, but not isolating it, leaving imprecision in the initial iron precursor concentration. Iron (III) stearate proved a superior alternative, being a commercially available and an easily manipulated solid at room temperature. The assumption that the absence of the alkene moiety in the oleate ligands upon replacement with stearate would bear little to no impact on the reduction potential and decomposition mechanism proved seemingly true given synthesis from ferric stearate yielded the desired magnetite phase under similar reaction conditions to previously reported methods. XRD data confirmed the magnetite phase as the only present phase and is presented in Figure 2.3 for a representative synthesis, showing iron (III) stearate as a viable precursor.

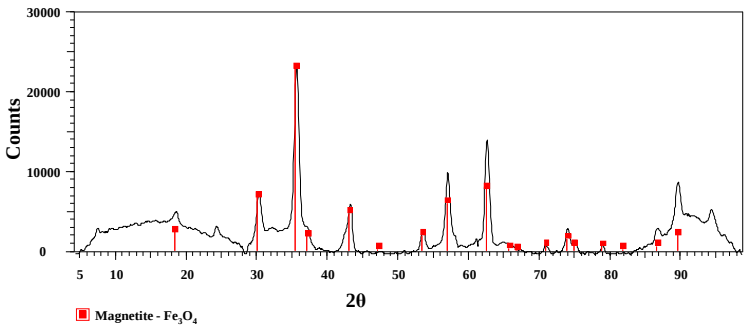

Figure 2.3 X-Ray Diffraction of as synthesized IONPs. Magnetite is the only phase observed

2.3.2. Kinetic Dependence of Nucleation on Surfactant Concentration.

Nucleation during LaMer's classic growth model occurs according to a nucleation rate function, $\Gamma(t)$, and can be approximated by a Gaussian function as presented in Figure 2.4. The

total number of nuclei, and thus the number of particles, is given by integration with respect to time. While the particle size does depend on the peak rate value, the duration of nucleation window, Δt_n, exerts control on the final average and standard deviation of particle diameters. For functions with comparable Δt_n values as in (A) and (B), (A) will yield smaller particles due to the larger maximum nucleation rate, with similar variance in both. For functions with comparable Γ_{max} values as in (B) and (C), the longer Δt_n for (C) will yield a broader distribution in particle diameter in addition to larger average particle diameters.[13]

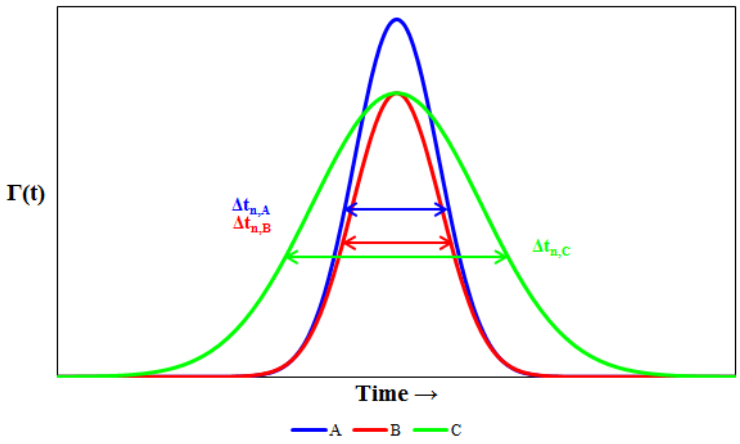

Figure 2.4 Example nucleation rate functions for LaMer's classical growth mechanism. Figure adapted from Buhro et al.[13]

As outlined above, modification to the duration of the nucleation window bears consequence on both the mean and variance in particle diameter. At constant temperature the effect of varying surfactant concentrations on Δt_n was observed. Table 2.1 and Figure 2.5 show the effect of surfactant concentration on the nucleation period. Within the range of concentrations examined, a linear response was observed. These results can be interpreted as the ligand in this system having an inhibitory effect on the nucleation event. Kinetically, once monomeric Fe_3O_4 is formed during decomposition, two possible outcomes in solution are nucleation or coordination by a ligand. As the ligand concentration is increased, the more

kinetically probable event becomes an association-disassociation event with oleic acid, leading to a prolonged nucleation period.

Surfactant Concentration Effects on the Nucleation Window				
Ratio	[Fe(stearate)$_3$] (mmolal)	[Oleic Acid] (mmolal)	T (°C)	Δt_n (s)
1:4	56.4	223	321	1560
1:5	56.4	280	321	2400
1:8	56.4	446	321	3277
1:10	56.4	564	321	4740

Table 2.1 Observed nucleation window times with varying surfactant concentrations.

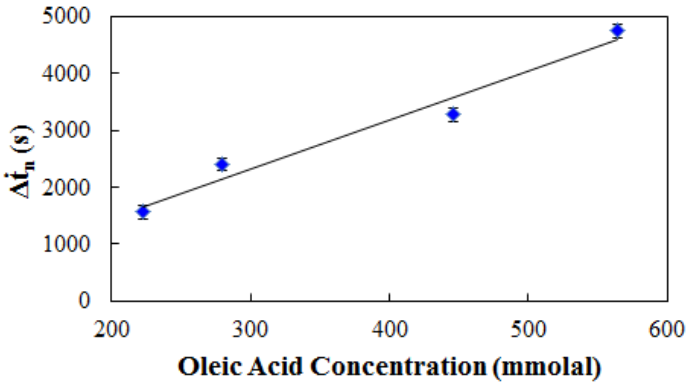

Figure 2.5 Effect of ligand concentration on the nucleation window time. A linear dependence is observed, with a coefficient of determination of 0.96 and an error in the slope of ± 1.1 s/mmolal

2.3.3. Particle Diameter Dependence on Surfactant Concentration.

A previous report utilizing amine-based surfactants showed decreasing particle sizes as ligand concentration increased;[18] however, no investigations into the similar effects for a carboxylic acid-based ligand with an iron (III) precursor have been conducted to our knowledge. Table 2.2 presents the cases studied here, with example micrograms presented in Figure 2.6. Particle diameters from ~8-16 nm were tuned by varying ligand concentrations at a constant iron (III) stearate concentration. Additionally, standard deviations in particle populations were observed from ~2-4 nm, also increasing with ligand concentration as the nucleation window increased in duration.

Surfactant Concentration Effects on Mean Particle Diameter					
Ratio	1:2	1:3	1:4	1:5	1:10
[Fe(stearate)$_3$] (mmolal)	56.4	56.4	56.4	56.4	56.4
[Oleic Acid] (mmolal)	112	167	223	280	564
Mean Diameter (nm)	8.31	8.90	10.02	11.04	15.44
Standard Deviation (nm)	2.39	2.71	2.68	2.37	4.15

Table 2.2 Average particle diameters and standard deviations in response to varying surfactant concentration at a thermal annealing time of 1 hour at 321°C, following nucleation

A linear dependence between the resultant particle diameter and the initial surfactant concentration was observed (Figure 2.7), supporting the approximation of the nucleation rate function as a Gaussian-type function whose width, Δt_n, bears an impact on both the particle population's mean diameter and the standard deviation. A correlation in the response of the latter based on surfactant concentration was observed, notably when the ratio of iron precursor-to-surfactant is adjusted to 1:10. However, the data did not immediately follow a specific trend. Further trials outside the range investigated here may elucidate this trend.

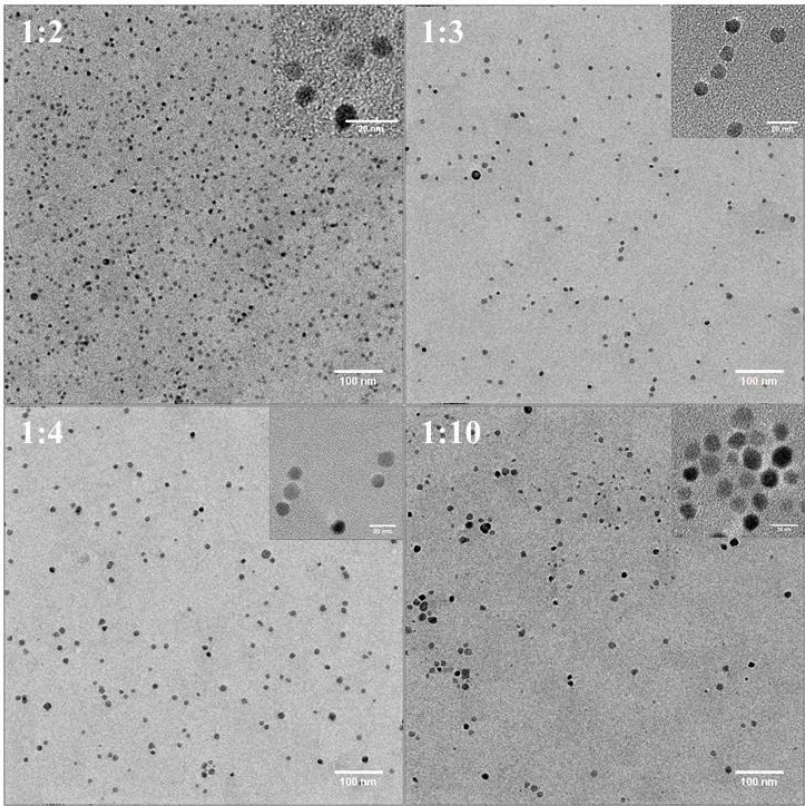

Figure 2.6 Transmission Electron Micrograms for as synthesized iron oxide nanoparticles

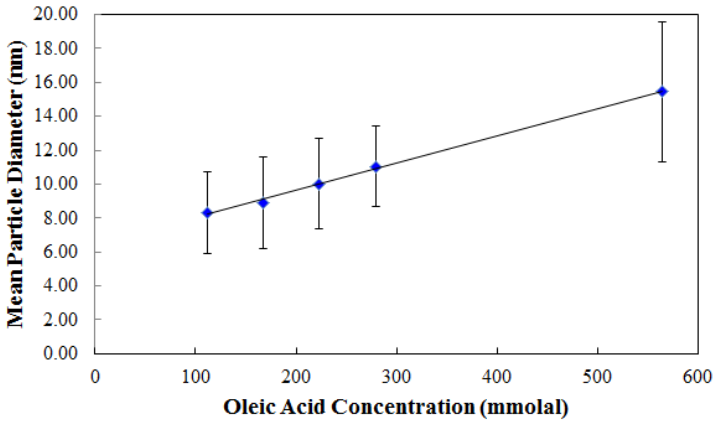

Figure 2.7 Effect of ligand concentration on mean particle diameter

From Figure 2.5 and Figure 2.7, along with an increase in the standard deviation of each particle distribution with increasing ligand concentration, one concludes that increased ligand concentration inhibits nucleation, increasing Δt_n and giving rise to larger resultant particles during primary nucleation prior to diffusional growth. While not immediately investigated, the data suggests that Γ_{max} was impacted by changes in ligand concentration. Thorough investigation of this effect would require a spectrochemical method of analysis and was beyond the scope of this project. Due to the magnitude of the error in the mean diameter for each trial, additional trials outside the investigated surfactant range could be investigated to more confidently conclude the linearity of the relationship between surfactant concentration and mean particle diameter.

2.3.4. Effects of Annealing Time on Particle Diameter.

Table 3 provides the average particle diameter for several precursor-to-surfactant ratios at varied annealing times. After nucleation, crystal growth continues by diffusion onto existing nuclei according of LaMer theory. Since the total number of nanoparticles is governed by the nucleation event, it is expected that annealing in solution during growth by diffusion will lead to larger average particle diameters. Indeed, this is what is observed for the system reported here.

Annealing Time (hours) Effects on Mean Particle Diameter (nm)				
Ratio	t = 0*	t = 1	t = 3	t = 6
1:2	6.94 ± 1.00	8.31 ± 2.48	8.72 ± 2.47	9.08 ± 2.08
1:5	9.18 ± 1.09	11.04 ± 2.37	11.17 ± 2.02	11.07 ± 1.77
1:10	10.35 ± 2.65	15.44 ± 1.97	15.82 ± 2.15	15.08 ± 3.56

*An annealing time of zero hours is labeled nominally; mathematically, this should be handled as an annealing time of approximately one minute, as was used in Figure 2.8.

Table 2.3 Average particle diameter with varying thermal annealing times for initial iron (III) stearate concentrations of 56.4 mmolal

As one model for crystal growth by diffusion following nucleation, Ostwald Ripening predicts that crystal size will increase linearly with longer annealing times. That mathematical model is given by Equation 2.1, where R_t is the particle radius at time t, γ is the surface energy, c_∞ is the solubility, υ is the material's molar volume, D is the material diffusion coefficient, R is the gas constant, and T is the temperature.[19]

$$\langle R_t \rangle^3 = \frac{8\gamma c_\infty \upsilon D}{9RT} t + \langle R_0 \rangle^3$$

Equation 2.1 Ostwald Ripening model for crystal growth by diffusion

While the mean radius cubed did generally increase over time, the response was not linear over the time investigated. Ostwald Ripening is a thermodynamically driven process and predicts that a singular large particle would eventually be achieved with sufficient annealing time via diffusional growth. However, the plot of the mean radius cubed versus annealing time shows increasing but somewhat asymptotic behavior at six hours in the cases studied, suggesting that Ostwald Ripening is at a minimum not the only growth mechanism following nucleation and that some other model is followed.

Other crystal growth models have been proposed empirically in the form of Equation 2.2, where m (the grain growth exponent) and k are both temperature dependent, and k follows the Arrhenius equation.[20]

$$\langle R_t \rangle^{\mathrm{m}} = \mathrm{k}t + \langle R_0 \rangle^{\mathrm{m}}$$

Equation 2.2 Empirical crystal growth modeling

However, the relation $R_t >> R_0$ is typically assumed for all t and the initial radius term is discarded. Noting that k is a temperature dependent Arrhenius coefficient and taking the logarithm of both sides then yields Equation 2.3, allowing for the determination of m (and the activation energy if temperature dependent trials are conducted).

$$\ln\langle R_t \rangle = \frac{1}{\mathrm{m}}\ln(A) - \frac{E_a}{R} * \frac{1}{T} + \frac{1}{m}\ln(t)$$

Equation 2.3 Application of the Arrhenius equation to empirical growth models

Figure 2.8 plots the 1:2, 1:5, and 1:10 trials utilizing Equation 2.3, with all trials done at 321°C. While Equation 2.3 serves as a useful model for the growth of magnetite NP in this system at low oleic acid concentrations relative to the iron precursor (m=22.2 ± 0.3 for the 1:2 trial), the diminished utility of this model at increasing initial surfactant concentrations suggests the surfactant plays a more complicated role in post-nucleation growth, requiring further investigation for precise modeling.

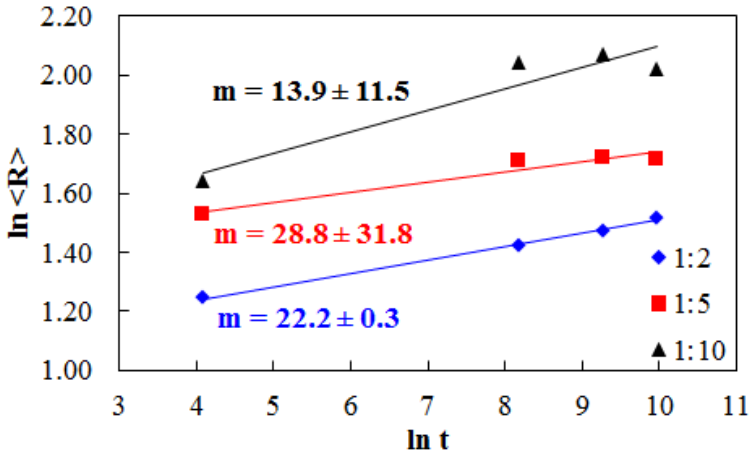

Figure 2.8 Nanoparticle growth modeling for 1:2, 1:5, and 1:10 initial iron:oleic acid ratios

2.4. Conclusions

Magnetite (Fe_3O_4) nanoparticles with good monodispersity were successfully synthesized from iron (III) stearate as a commercially available and economical precursor. The nucleation period was found to depend proportionally on the initial surfactant concentration, presenting an alternative to previously reported results utilizing amine-based ligands. Control over particle diameter is achievable by varying iron precursor-to-surfactant ratios, and for this system, increasing oleic acid concentration relative to iron (III) stearate yielded larger particles with larger deviations in particle diameter within the sample, an observation consistent with an observed increase in the nucleation window. Initial growth modeling during annealing for this system suggests an empirical model other than Ostwald Ripening is followed and that surfactant concentration bears some consequence on crystal growth following nucleation. The reproducibility of this synthetic approach is critical moving forward into surface functionalization and sensor design in order to optimize the glucose biosensor.

3. Nanoparticle Surface Functionalization

3.1. Introduction

Critical aspects of a viable glucose biosensor are its sensitivity, limit of detection, shelf-stability, and biocompatibility. The sensitivity and limit of detection of the assay will be dependent on the amount of active glucose oxidase present, and this will be addressed mathematically in Chapter 4. Shelf-life, particularly the stability and sustained activity of glucose oxidase, are necessary if an *in vivo* amperometric sensor is to be implanted in tissue without diffusional loss of enzyme. The foreign body response to implanted electrodes in mammalian brain tissue is known and continues to be examined, specifically the development of scar tissue around the sensor that causes a loss of sensitivity over time.[21] By reducing the size of the electrode to tens of microns in diameter, it is the goal of this work to ultimately reduce that response, although it will not be avoided entirely.

While the Transmission Electron Microscopy data presented in Chapter 2 is useful for examining the synthetic control over the nanoparticle core, these measurements are made *in vacuo.* From a practical standpoint, the behavior of the nanoparticles in a solution phase must be considered. Dynamic Light Scattering (DLS) measurements serve this purpose, and details of this technique can be reviewed elsewhere.[22] Briefly, DLS auto-correlates time-varying scattering intensities due to Brownian motion to determine the particles' average diffusional coefficient in a particular solvent. The Stokes-Einstein equation can then be used in the form of Equation 3.1, provided the particles are approximated as spheres, as was assumed in Chapter 1.

$$D = \mu k_B T = \frac{\mu_q k_B T}{q} = \frac{k_B T}{f} = \frac{k_B T}{3\pi\eta d}$$

Equation 3.1 Stokes-Einstein equation for a spherical particle

The diffusional coefficient, D, in a given solvent with a viscosity, η, at a temperature, T, allows one to measure the hydrodynamic diameter, d. The hydrodynamic diameter as measured via DLS provides complementary information to that obtained via TEM, measuring diameter inclusive of the particle core and solvation shell. If the particle surface is charged, the solvation shell will contain both solvent molecules and bound counter-ions, as shown in Figure 3.1.[23]

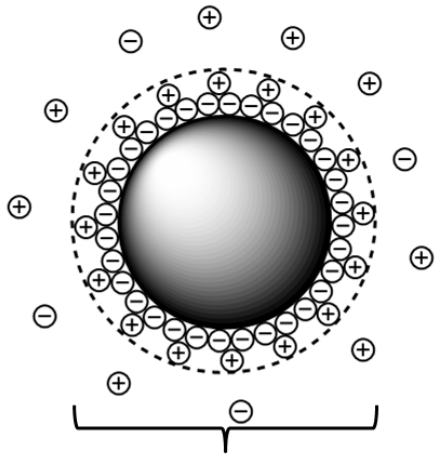

Hydrodynamic diameter for a negatively charged nanoparticle with bound counter-ions within the solvation shell (dashed line), surrounded by the diffusional layer of solvent and free ions. The ζ potential is the electrostatic potential measured at this distance, and is negative as illustrated in the case here.

Figure 3.1 Solvation shell for a charged particle[23]

Knowing the diameter and provided the particle surface is charged, electrophoretic light scattering can then be used to measure the ionic mobility, μ_q, and the ζ potential at the interface between the solvation shell and the diffusional layer surrounding the particle. Ultimately, the amount of charge per particle, q, from Equation 3.1 will be useful to estimate the number of particles, or the number of particle-enzyme bioconjugates, deposited into a sensor during electrodeposition, as will be discussed in Chapter 4. The ζ potential is also a measure of colloidal stability in charged particles, where greater absolute values of the ζ potential, typically on the order of 0-100 mV, suggest a greater resistance against aggregation. It should be noted that the electrophoretic properties of the particles will be dependent on the pH of the suspension.

However, as synthesized magnetite NPs in Chapter 2 present a hydrophobic surface, with the iron oxide core coordinated by oleic acid ligands, requiring functionalization to achieve both water solubility for utility in biological applications and appreciable surface charge for the purposes of device fabrication via electrodeposition. Multiple biocompatible surface coatings have been explored and reviewed in the literature,[10] with polyethylene glycol (PEG), dextran, and silica coatings being the most prevalent. While widely used in drug delivery, imaging contrast enhancement, and hyperthermia-induced necrosis in cancer treatment, PEG does not provide a sufficiently high number of sites for covalent enzyme attachment or charge generation as required by this project, having only two functionalization sites.[24] Robust glucose oxidase-dextran conjugates are known and do provide a reasonable option;[25] however, the presence of an iron (II) center in magnetite raises concern for generation of reactive oxygen species *in vivo*, making it desirable to completely encapsulate and passivate the particle core. This also eliminates the possibility of a conventional small ligand exchange to replace hydrophobic ligands with hydrophilic ones. To achieve complete core passivation and to generate a large number of binding sites, a modified silica coating was selected. Amino and other silane derivatives are commercially available and have been used to generate water-soluble nanoparticles.[26] For this work, (3-aminopropyl)trimethoxysilane was selected, and Figure 3.2 illustrates how the condensation reaction proceeds for both this silane and tetraethoxysilane, used below.

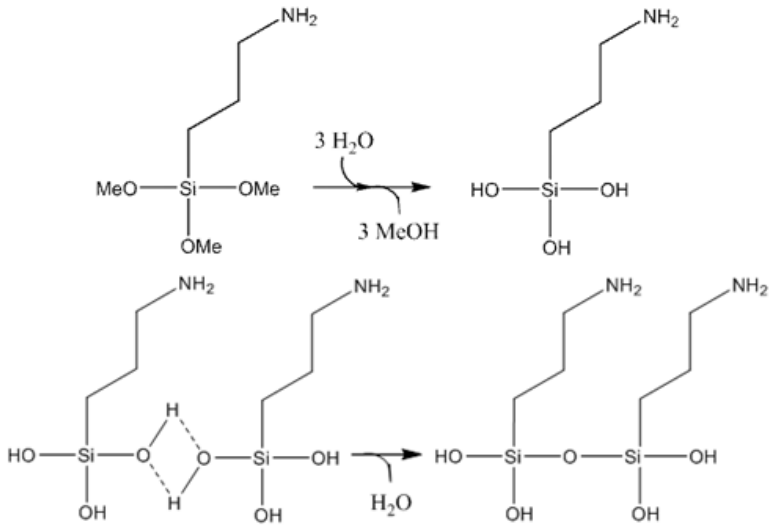

Figure 3.2 Silane Condensation

At a biologically relevant pH, the above surface functionalization scheme should result in slightly positive ζ potentials for amino surfaces based on the pKa of aliphatic amines being 10-11. This work would preferentially utilize a positive deposition potential, based on the capillary electrode design, and known carbodiimide/N-hydroxysuccinimide mediated coupling chemistry for enzyme attachment.[27] A carboxylic acid surface functionalization would provide for both at biological pH, and can be accomplished by a nucleophilic cyclic anhydride ring opening reaction (Figure 3.3).[28]

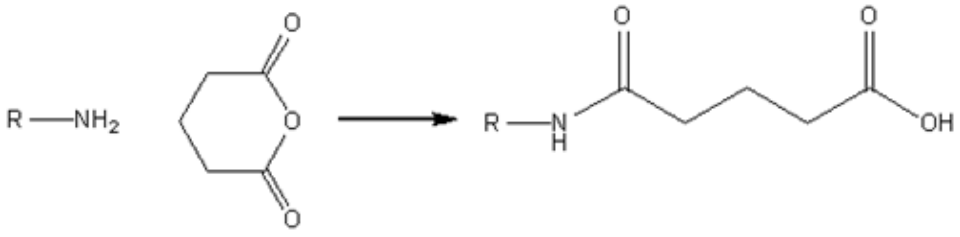

Figure 3.3 Nucleophilic Ring Opening for glutaric anhydride

It should be noted that hydroxyl functionalities on a silica surface could also serve as the nucleophile in Figure 3.3, resulting in the generation of an ester linkage. However, an amide linkage to the nanoparticle surface, and ultimately to the conjugated enzyme, will be less susceptible to hydrolysis than an ester linkage, ultimately improving the robustness of the sensor.

The ultimate synthetic goal to this point is the generation of a monodisperse suspension of functionalized magnetite nanoparticles with a high surface density of carboxylate functionalities, presenting a substantially negative ζ potential on the order of approximately -30 mV or less that will provide for efficient electrodeposition under a positive bias while also being a measure of the colloidal stability of the particles in the suspension.

3.2. Materials and Methods

3.2.1. Materials

Tetraethoxysilane (TEOS), (3-aminopropyl)trimethoxysilane (APTS), polyoxyethylene (5) nonylphenylether (IGEPAL CO-520), glutaric anhydride, succinic anhydride, sodium phosphate tribasic dodecahydrate, and cyclohexane were from Sigma-Aldrich and used without further purification. Deionized water was further purified utilizing a Barnstead Nanopure II RO System.

3.2.2. Instrumentation

Dynamic and electrophoretic light scattering measurements were made on a Brookhaven ZetaPALS instrument equipped with the BI-MAS module for particle sizing. Dispersions were measured at concentrations of 0.1-0.5 mg/mL in nanopure water.

The infrared spectrum if Fe_3O_4@TEOS/APTS NPs was collected utilizing a PerkinElmer Spectrum 100 FT-IR Spectrometer with a resolution of 1 cm^{-1}. Amino-functionalized nanoparticles were made into powders by drying overnight in a desiccator, and KBr pellets were made by a hand press.

3.2.3. Silica Coating and Amino-Functionalization of Magnetite Nanoparticles

3000 μL of IGEPAL CO-520 were added to 50 mL of cyclohexane and allowed to stir on a magnetic stir plate under air for 5 minutes to allow for micelle formation. 80 mg of oleic acid

stabilized IONPs (as synthesized in Chapter 2) were then added and allowed to stir another 5 minutes to allow for migration of the nanoparticles into the micelles. 3000 μL of TEOS were then added to the mixture and allowed to stir for 5 minutes. Lastly, 0.1 mL of 28-30% ammonium hydroxide was added to catalyze the condensation. The resulting mixture was allowed to stir under air at room temperature for 24 hours. To the resulting suspension, 20 mL of acetone were added and the product was isolated by centrifugation.

The product was then suspended in 60 mL of absolute ethanol. 1000 μL of APTS were added. Subsequently, 0.2 mL of 28-30% ammonium hydroxide was added and the mixture was stirred for 24 hours. The product was then collected via centrifugation without the use of a flocculent. The supernatant was discarded and the product was washed with 1:1 nanopure water:isopropyl alcohol three times with centrifugation. The amino-functionalized particles were then suspended in nanopure water with moderate bath sonication.

3.2.4. Carboxylate-Functionalization via Anhydride Ring Opening

This protocol was adapted from a procedure utilizing molecular amines as the nucleophile and was similar for both succinic and glutaric anhydrides.[28] 500 mg of Fe_3O_4@TEOS/APTS was easily suspended in 20 mL of 0.25 M sodium phosphate buffer at pH 7.2. 0.5080 g or 0.4498 g of glutaric or succinic anhydride, respectively, were added to the suspension and magnetically stirred for 3 hours. 10 mL of isopropyl alcohol were added and the product was isolated by centrifugation. Product was ultimately suspended in 20 mL of nanopure water, and these suspensions were utilized in Chapter 4 for enzyme conjugation.

3.3. Results and Discussion

An early attempt to coat magnetite particles synthesized by replicating the work of Peng et al.[16] with an amino-functionalized silica shell via TEOS/APTS condensation had yielded the results observed in Figure 3.4.

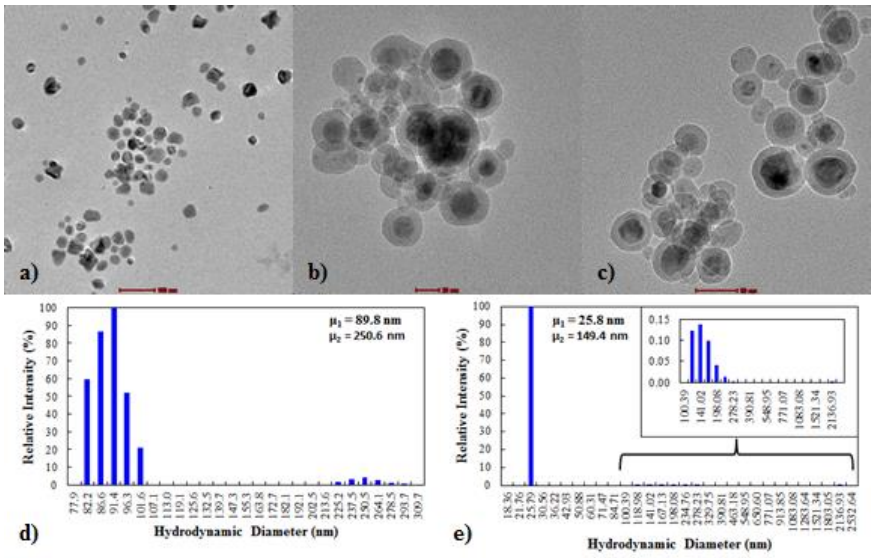

Figure 3.4 Fe_3O_4 (a), Fe_3O_4@TEOS (b and d) and Fe_3O_4@TEOS/APTS (c and e) NPs. Magnetite cores were synthesized according to Peng et al.[16]

As seen in Figure 3.4a), the magnetite nanoparticle population was qualitatively polydisperse compared to the mean diameter of 35 nm reported by Peng.[16] This variance in the diameter along with the laborious nature of the synthesis birthed the work presented in Chapter 2. Silica and amino functionalizations, Figure 3.4b) and c) respectively, yielded reasonably constant silica shell thicknesses on the order of 10 nm for each particle. However, passivated particles aggregated, which was confirmed by both electron microscopy and dynamic light scattering measurements for both Fe_3O_4@TEOS and Fe_3O_4@TEOS/APTS, presented in figure Figure 3.4b-e. This aggregation might be attributed to inter-particle hydrogen bonding between remaining hydroxyl groups and amine functionalities on the silica surface.

Prior to proceeding with the anhydride ring opening reaction presented in Figure 3.3, confirming the presence of the amine functionality was necessary, for which vibrational

spectroscopy was utilized. Specifically, the N-H bend, C-N stretch, and N-H wag were identified at 1634 cm-1, 1098 cm-1, and 810 cm-1 (See Figure 3.5), all consistent with primary aliphatic amines.[29] The two characteristic N-H stretch bands could not be resolved, and this was attributed to the likelihood of appreciable hydroxyl functionalities remaining on the particle surface following silane condensation, as well as potentially inadequate drying of the sample.

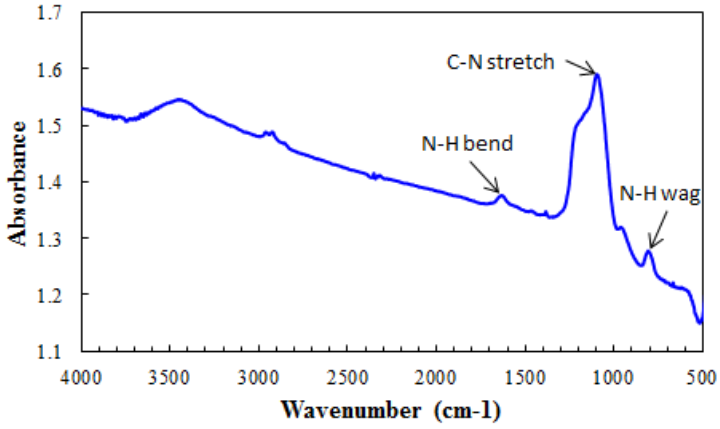

Figure 3.5 Mid-IR spectrum of Fe3O4@TEOS/APTS aggregates

Encouraged by spectroscopic confirmation of the amino group following silane condensation and the monodispersity of dispersions synthesized in Chapter 2, silica and amino derivatizations were attempted using particles synthesized according to Chapter 2. Utilizing IONPs that measured approximately 14 nm by TEM, multiple silica- and amino-functionalization attempts resulted in micron and larger aggregates, with DLS and electrophoretic light scattering results presented in Figure 3.6. Of note, the measured ζ potential of only -5.20 mV is reasonable for an amine at pH 7 as no appreciable surface charge is expected at this pH.

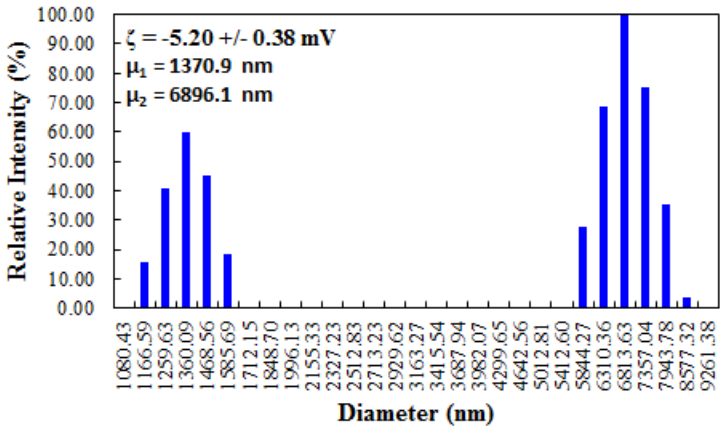

Figure 3.6 Polydispersity of Fe_3O_4@TEOS/APTS aggregates

This degree of aggregation is more complex and is improbably caused by hydrogen bonding alone. Regardless, the anhydride ring opening with succinic and glutaric anhydride was conducted utilizing these > 1 μm aggregates, yielding the DLS spectra and ζ potentials in Figure 3.7. As expected upon conducting the cyclic anhydride ring opening, the ζ potential increased in magnitude substantially, consistent with carboxylate functionalities on the particle surface at pH 7. The difference in ζ potential between a) and b) in Figure 3.7 might be that succinylation is thermodynamically more favorable than glutarylation given the increased conformational strain in succinic anhydride over glutaric anhydride.[30] This would improve the favorability of product formation at equilibrium; however, this hypothesis can't be validated from the ζ potential alone.

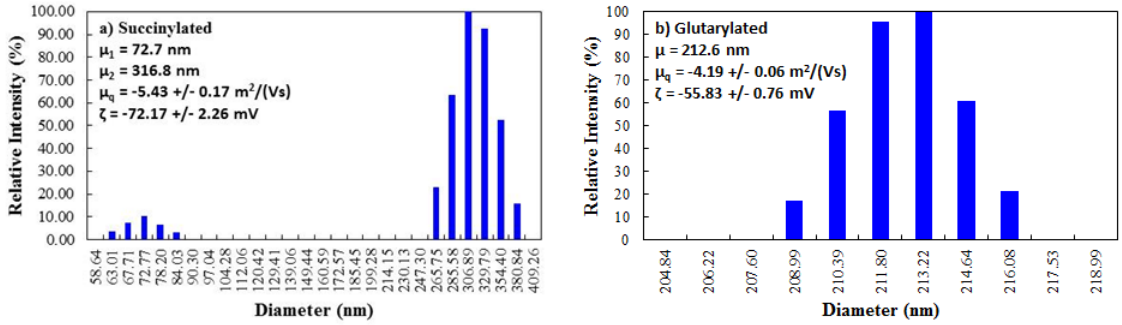

Figure 3.7 DLS Spectra for a) succinylated and b) glutarylated Fe_3O_4@TEOS/APTS aggregates

Interestingly, a decrease in in the hydrodynamic diameter was observed in both cases, calling into question the covalency of the interactions causing aggregation in comparison to the diameter as measured by TEM. To investigate this, Fe_3O_4@APTS aggregates were synthesized (forgoing the initial silica coating using TEOS), suspended in 1.0 mM Triton X-100 and compared to their DLS spectrum in nanopure water and the transmission electron micrograph (Figure 3.8). Removing the initial silica coating via TEOS condensation was done as it was thought the aggregation may be due to the TEOS having four points for covalent attachment to another silicon center, while the use of APTS alone would yield only three points. As shown in Figure 3.8a), this was not the case.

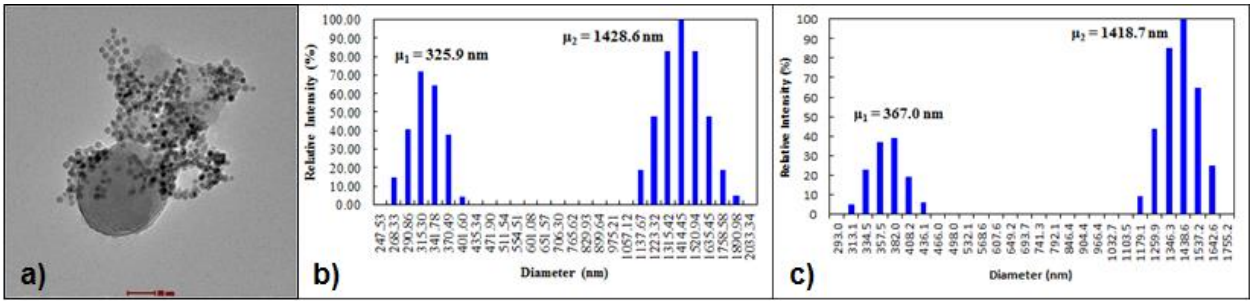

Figure 3.8 Fe_3O_4@APTS aggregate diameter comparison by a) TEM and DLS at pH 7 in b) nanopure water and c) 1.0 mM Triton X-100

Upon examining Figure 3.8, it is obvious from the electron microscopy results that the aggregation is not the result of interparticle hydrogen bonding; rather, the silica-like surface coated over numerous particles. The 300-400 nm aggregates as measured by DLS are consistent with TEM measurements.

These results suggest that the IONPs synthesized in Chapter 2 are behaving differently in solution than they are when drop casted on a TEM substrate, allowing solvent to evaporate for *in vacuo* measurements. To examine this, the TEM micrograph and DLS spectrum in hexane were compared (Figure 3.9). Indeed, the oleic acid stabilized IONPs do show aggregation in hexane, with a maximum aggregate diameter of roughly 1 μm.

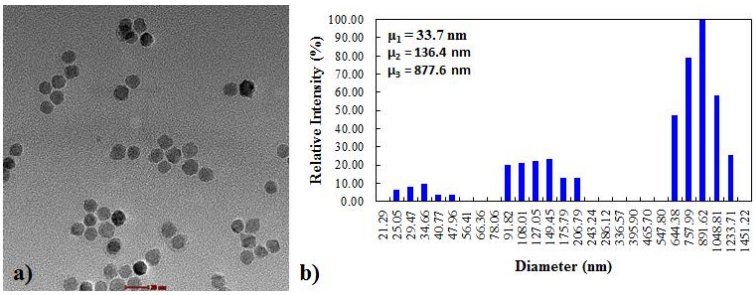

Figure 3.9 Comparison of as synthesized hydrophobic IONPs by a) TEM and b) DLS in hexane

It is reasonable to conclude that the aggregation observed in the surface functionalized iron oxide nanoparticles is due to aggregation of the hydrophobic IONPs prior to functionalization. The cause of this aggregation is unknown and was not studied here. Considering the nature of the surface of the oleic acid-stabilized Fe_3O_4, nanoparticles, London Dispersion forces alone are probably incapable of causing aggregation on the micron scale. A reasonable cause of this aggregation is that the magnetite nanoparticles have net magnetic moments leading to the observed aggregation. Acquiring the hysteresis curves for this material would elucidate this possibility, and this should be considered before pursuing this work further. Increased temperature and/or sonication prior to DLS measurements may provide a means to disrupt aggregation and yield a more monodisperse sample for use and should be examined, as well.

3.4. Conclusions

As synthesized iron oxide nanoparticles showed a tremendous deviation in dispersity between measurements made by TEM and DLS. The more applicable behavior in solution as measured by DLS revealed significant aggregation, generating multimodal, polydisperse suspensions of particles pre- and post-modification. The hydrodynamic diameters from DLS and widths of the silica-cross-linked as measured by TEM correlated to one another well and can be rationalized in terms of large aggregations of particles existing prior to functionalization. Future

surface functionalization efforts using the particles described in Chapter 2 should first return attention to solving the polydispersity problem that is observed in aqueous and organic suspensions of particles to ensure uniform surface coatings. Only then will reproducible charge carriers be realized for efficient electrodeposition of enzyme-nanoparticle bioconjugates.

4. Enzyme Conjugation and Sensor Design and Response

4.1. Introduction

Critical to the development of a biological sensor that utilizes an enzyme at its core is an understanding of enzyme kinetics. While typical solution-phase chemical kinetics based on collision theory often involve rates laws that show some linear (or perhaps quadratic) dependence on reactant concentration, catalytic and enzymatic reactions typically follow a more complex mechanism giving rise to a nonlinear dependence on reactant concentration. If *S* is the substrate of enzyme *E*, one possible mechanism is given by Equation 4.1.

$$E + S \underset{k_{-1}}{\overset{k_1}{\rightleftharpoons}} ES \overset{k_p}{\rightarrow} E + P$$

Equation 4.1 Single-substrate enzymatic mechanism

The binding of the substrate to the enzyme is fast to equilibrium and the rate determining step is the conversion of the substrate to product from the bound complex, giving back the free enzyme. Intuitively, the dependence of the initial rate on the substrate concentration will not be linear if *[S] > [E]* as the addition of substrate will not have free enzyme to bind to. As reviewed by Ault, the mathematical relationship yields a hyperbolic curve if tracked experimentally and follows Equation 4.2.[31]

$$rate = a\left(\frac{1}{1+\frac{b}{[S]}}\right) \text{ or } rate = a\left(\frac{[S]}{[S]+b}\right),$$

$$where\ \left(\frac{[S]}{[S]+\ b}\right) = fraction\ of\ enzyme\ bound\ by\ substrate$$

Equation 4.2 Rate law for a single-substrate enzyme that follows "Michaelis-Menten" kinetics[31]

Upon considering two cases, the physical meanings of *a* and *b* become apparent. When *[S]>>b*, the rate simplifies to *a*, representing the maximum rate (V_{max}) achievable by the enzyme under specific conditions (pH, ionic strength, temperature, etc.). In the case of *[S] = b*, the rate

becomes one half of V_{max}. The value of b is specially named the Michaelis constant, K_M, and follows from the steady state approximation for the complex ES and can be mathematically shown to yield Equation 4.3.

$$K_M = \frac{k_{-1} + k_p}{k_1}$$

Equation 4.3 Michaelis constant for a single-substrate enzyme

For the development of an electrochemical sensor where current is generated by an electrochemically active enzyme, the response to analyte is measured as a current whose amplitude is proportional to analyte concentration. If one assumes $K_M >> [S]$, then $[S]+K_M \approx K_M$ and the rate can be rewritten as Equation 4.4,

$$rate = V_{max}\left(\frac{[S]}{[S] + K_M}\right) \approx V_{max}\left(\frac{1}{K_M}\right)[S]$$

Equation 4.4 Single-substrate enzyme kinetics rate law when $K_M >> [S]$

and an initially linear response can be obtained with varying $[S]$. The challenge is to design an electrochemical enzyme-based sensor where the conditions are such that K_M is as large as possible to yield a wide linear dynamic range in the assay and where V_{max} is likewise as large as possible to produce enhanced sensitivity with changes in analyte concentration.

For the project presented here, the goal is the development of an *in vivo* glucose sensor utilizing glucose oxidase. Glucose oxidase (EC 1.1.3.4), as found in Aspergillus niger, is a 144 kDa dimeric enzyme whose active cofactor is flavin adenine dinucleotide (FAD). It is an oxido-reductase enzyme that follows a "ping-pong" mechanism (in Equation 4.5), where E is the enzyme, S is glucose, P_1 is the resulting δ-lactone, and oxygen is the final electron acceptor as it is converted to hydrogen peroxide, P_2.

$$E_{ox} + S \xrightarrow{k_1} E_{red}P_1 \xrightarrow{k_2} E_{red} + P_1 \text{ "ping"}$$

$$E_{red} + O_2 \xrightarrow{k_3} E_{ox}P_2 \xrightarrow{k_4} E_{ox} + P_2 \text{ "pong"}$$

Equation 4.5 Two-substrate enzymatic "ping-pong" mechanism

As a result, the rate law becomes more complicated and dependent not only on the concentration of glucose but also on the oxygen concentration. Rather than a singular $K_{M,}$ there is a Michaelis constant for both oxygen and glucose. Gibson et al. conducted stop flow experiments to determine these values along with the corresponding V_{max} at varying temperatures.[32] At 38ºC, Gibson reported V_{max}, $K_{M(oxygen),}$ and $K_{M(glucose)}$ values of 2000 M sec^{-1}, 0.83 mM, and 120 mM, respectively. At a biologically hypothermic, but laboratory-relevant, temperature of 27ºC, those values decreased to 1150 M sec^{-1}, 0.48 mM, and 110 mM. Daily blood glucose concentrations range from 3-20 mM in diabetic patients, well below the $K_{M(glucose)}$ for glucose oxidase. Similarly, normal venous blood concentrations for oxygen are approximately 1-2 mM, approximately twice that of the published $K_{M(oxygen)}$ value. Gibson showed that the conversion of hydrogen peroxide back to molecular oxygen is the rate limiting step in the "ping-pong" mechanism for glucose oxidase. The rate law consistent with Gibson's work is given below in Equation 4.6.

$$rate = \left(\frac{1}{\frac{1}{V_{max}} + \frac{1}{k_1[Glucose]} + \frac{1}{k_3[O_2]}} \right), V_{max} = \frac{k_2 k_4}{k_2 + k_4} at\ infinite\ [Glucose] and\ [O_2]$$

Equation 4.6 Inverted rate law for Glucose Oxidase

So for a viable glucose biosensor, oxygen saturation is critical to ensure that change in an observed rate is due to change in glucose concentration. This allows one to discard the oxygen-dependent term, and the rate law from Equation 4.6 simplifies to the single substrate model

presented in Equation 4.4, provided the glucose concentration is far less than its respective Michaelis constant.

By recognizing that the response of the sensor could possibly be limited by local oxygen concentration and given the modest reduction potential of oxygen given by Equation 4.7,[33] an electrochemical biosensor can be designed to make amperometric measurements below that potential with a working platinum electrode whose surface has been electrodeposited with the nanoparticle-enzyme bioconjugates.

$$O_2 + 2H^+ + 2e^- \rightleftharpoons H_2O_2, \qquad E^\circ = 0.695\ V$$

Equation 4.7 Reduction Potential for Molecular Oxygen

As a result, hydrogen peroxide serves as both the species for amperometric detection and a source of molecular oxygen at the electrode surface, which would oxidize $FADH_2$ back to FAD and render the enzyme active. This overcomes the possibility of an oxygen-limited scenario, holding the oxygen concentration reasonably high and constant during analysis to achieve a linear response. The design of the electrode is given in Figure 4.1.

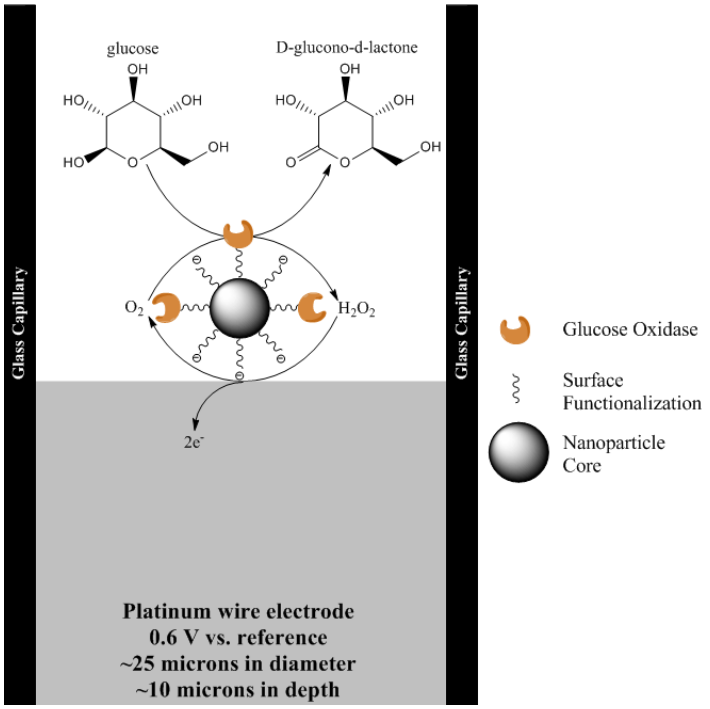

Figure 4.1 Amperometric glucose biosensor design, based on the enzymatic cycle of glucose oxidase

4.2. Materials and Methods

4.2.1. Scanning Electron Microscopy (SEM) and Energy Dispersive X-ray (EDX) Analysis

SEM imaging and Energy Dispersive X-ray (EDX) of fabricated sensor cavities were made utilizing a Carl Zeiss Leo 1550 Field Emission Scanning Electron Microscope. Sensors were mounted at ~45° and secured to the holder utilizing ample copper tape to improve the conductivity of the sensors to the stage and prevent charge accumulation and improve image contrast. Raster scanning was not conducted for elemental mapping due to charge accumulation. Rather, localized bulk EDX measurements were confined to the areas indicated in Figure 4.2.

4.2.2. Enzyme-Nanoparticle Conjugation

The protocol for glucose oxidase conjugation was adapted from the literature and conducted by Dwight Deay in Dr. Mark Richter's research group at the University of Kansas.[28] Glutarylated or succinylated Fe_3O_4@TEOS/APTS aggregates were isolated by centrifugation and

suspended in 0.1 M sodium phosphate buffer at pH 7.2. To this suspension, 1-ethyl-3-(3-dimethylaminopropyl)carbodiimide (EDC) and N-hydroxy-succinimide (NHS) were added to 3 μM and 4 μM, respectively. This suspension was agitated by mechanical turning for 4 hours @ 4°C. The activated aggregates were then isolated by centrifugation to remove excess coupling agent and suspended in 0.1 M phosphate buffer at pH 7.2. Trials were also conducted at 300 μM and 400 μM EDC and NHS, respectively.

Glucose oxidase was added to this suspension @ 4°C and the reaction mixture was agitated by mechanical turning for 24 hours. After this period, the functionalized aggregates were washed by centrifugation three times using fresh buffer, and then finally suspended in the same. To prevent bacterial growth, 0.01% sodium azide was added.

4.2.3. Electrode Fabrication and Bioconjugate Electrodeposition

Glass/platinum capillary electrodes are the property of and were fabricated by Mr. Donald Gwartney and Dr. Peter Petillo of Pinnacle Technology Inc., Lawrence, KS. This technique is covered by US Patent Application US 2013/0324820 A1.[34] Following fabrication but prior to bioconjugate deposition, the sensor cavities were cleaned to remove solid debris remaining from the fabrication process. Sensors were placed in a Pyrex bottle with a solution of 1:1:1 nanopure water:ethanol:acetone and sonicated in a bath sonicator (Bransonic Ultrasonic) for 20 seconds. Capillary substrates were then photographed under an optical microscope.

4.2.4. Biosensor Response to Glucose

Glucose response testing was performed by Donald Gwartney of Pinnacle Technology Inc. on the University of Kansas with the material and practical assistance of Dr. George Wilson. A stock solution of 0.5 M glucose was prepared. A beaker was filled with 40 mL of 0.1 mM PBS buffer and magnetically stirred at room temperature. A functional biosensor was placed

into the solution. A CH Instruments 6205c Electrochemical Analyzer was utilized to measure current at a constant applied voltage of 0.6 V relative to a Ag/AgCl reference electrode and data was collected utilizing the provided CH Instruments software.

After achieving a stable baseline current, serial injections of 80 μL of 0.5 M glucose (representing a 1.0 mM increase in glucose in the testing solution) were made to the 40 mL test buffer solution and current was recorded for approximately 30 seconds between injections.

4.3. Results and Discussion

4.3.1. Electrode Analysis

Prior to deposition, electrodes were analyzed by SEM and EDX in order to determine cavity depth and chemical composition in order to understand the environment into which bioconjugates would be deposited. The use of strongly basic solutions with high cyanide solutions during cavity etching and washing make it possible that deposited enzyme would be subjected to high alkalinity, potentially adversely affecting the enzyme's activity and ultimately reducing the sensitivity of the biosensor, making it necessary analyze the deposition and glass capillary surfaces prior to deposition. Figure 4.2 shows that electrodes had non-uniform surfaces with substantial sodium, potassium, and nitrogen signals prior to rinsing (a-c). Rinsing steps significantly cleared solid traces of cyanide and hydroxide salts of sodium and potassium, generating reproducible electrode surfaces and cavity depths (Figure 4.2 d-f). Depths of the rinsed cavities were calculated using the stage angle of 45° to be 10-11 μm, consistent with optical measurements made by Pinnacle Technologies Inc., who also showed this depth was adjustable by varying their etching conditions.

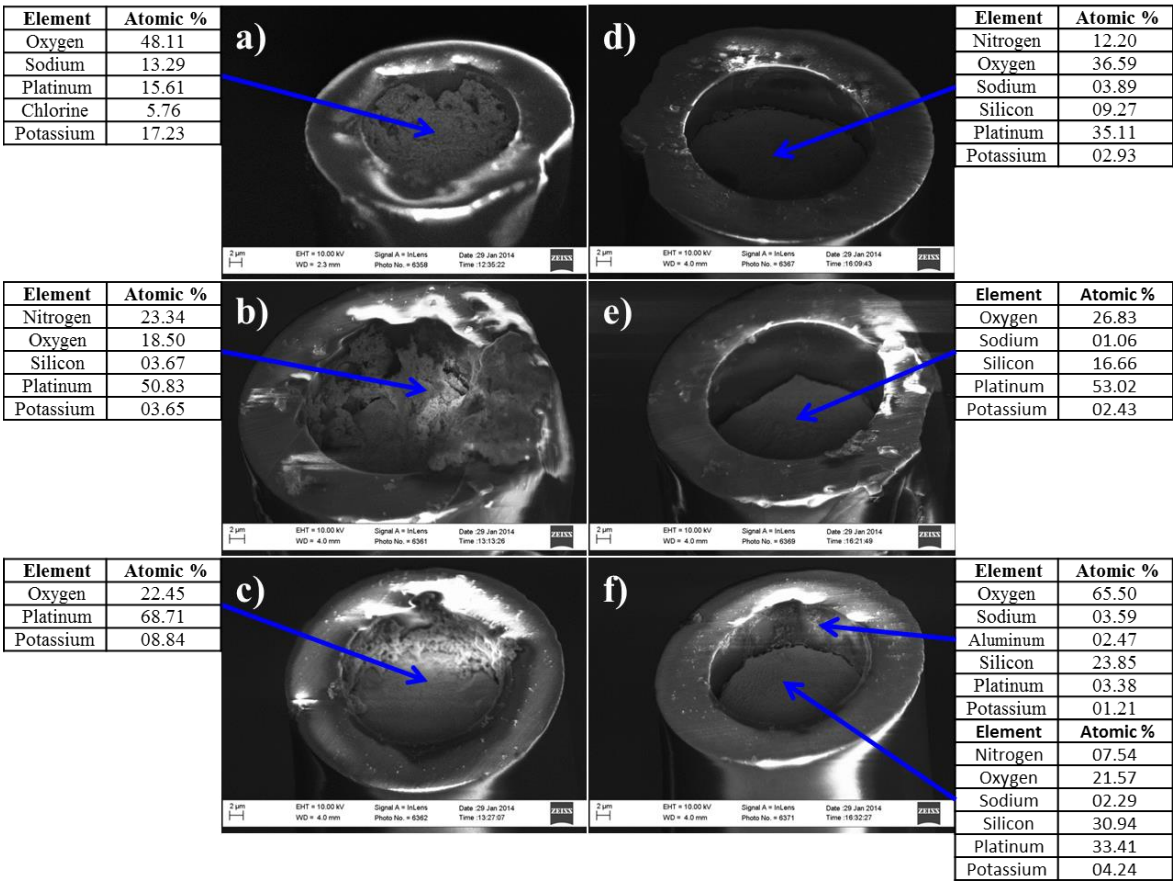

Element	Atomic %
Oxygen	48.11
Sodium	13.29
Platinum	15.61
Chlorine	5.76
Potassium	17.23

Element	Atomic %
Nitrogen	12.20
Oxygen	36.59
Sodium	03.89
Silicon	09.27
Platinum	35.11
Potassium	02.93

Element	Atomic %
Nitrogen	23.34
Oxygen	18.50
Silicon	03.67
Platinum	50.83
Potassium	03.65

Element	Atomic %
Oxygen	26.83
Sodium	01.06
Silicon	16.66
Platinum	53.02
Potassium	02.43

Element	Atomic %
Oxygen	22.45
Platinum	68.71
Potassium	08.84

Element	Atomic %
Oxygen	65.50
Sodium	03.59
Aluminum	02.47
Silicon	23.85
Platinum	03.38
Potassium	01.21

Element	Atomic %
Nitrogen	07.54
Oxygen	21.57
Sodium	02.29
Silicon	30.94
Platinum	33.41
Potassium	04.24

Figure 4.2 Scanning Electron Microscopy and Energy Dispersive X-ray Spectroscopy of Representative Electrodes

4.3.2. Electrodeposition of Fe_3O_4@TEOS/APTS-GOx Bioconjugates

During deposition, current was monitored and collected. Figure 4.3 is a representative curve for Fe_3O_4@TEOS/APTS-GOx bioconjugates, generated utilizing glutaryl and succinyl linkers as described in Chapter 3.

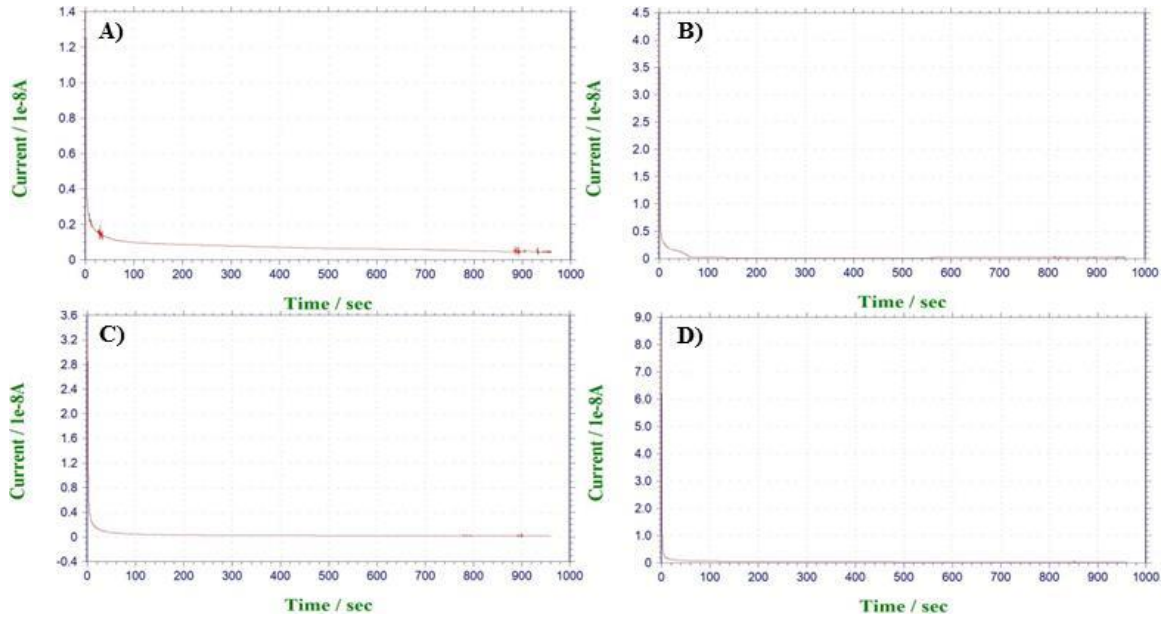

Figure 4.3 Current vs. time curves for electrodeposition of glutarylated (A-B) and succinylated (C-D) Fe_3O_4@TEOS/APTS NPs coupled to GOx under harsh (300 µM EDC/400 µM NHS, A and C) and mild (3 µM EDC/4 µM NHS, B and D) coupling conditions.

All observed depositions displayed rapid declines in current initially, approaching nearly constant currents on the order of a 1 nA after approximately 2 minutes of deposition. A potential cause of the decrease in current is the formation of a resistive layer of bioconjugate material at the electrode surface within the cavity. Another likely contribution to the decay in the current would be the negative surface charge of the bioconjugates causing coulombic repulsion of further deposition after an initial layer of bioconjugates has deposited.

The decay of the current, considered alone, might suggest that the electrode cavity has been completely filled with bioconjugates; however, monitoring charge accumulation over time as well as post-deposition optical micrograms of the same electrodes from Figure 4.3 counter this possibility and are presented in Figure 4.4.

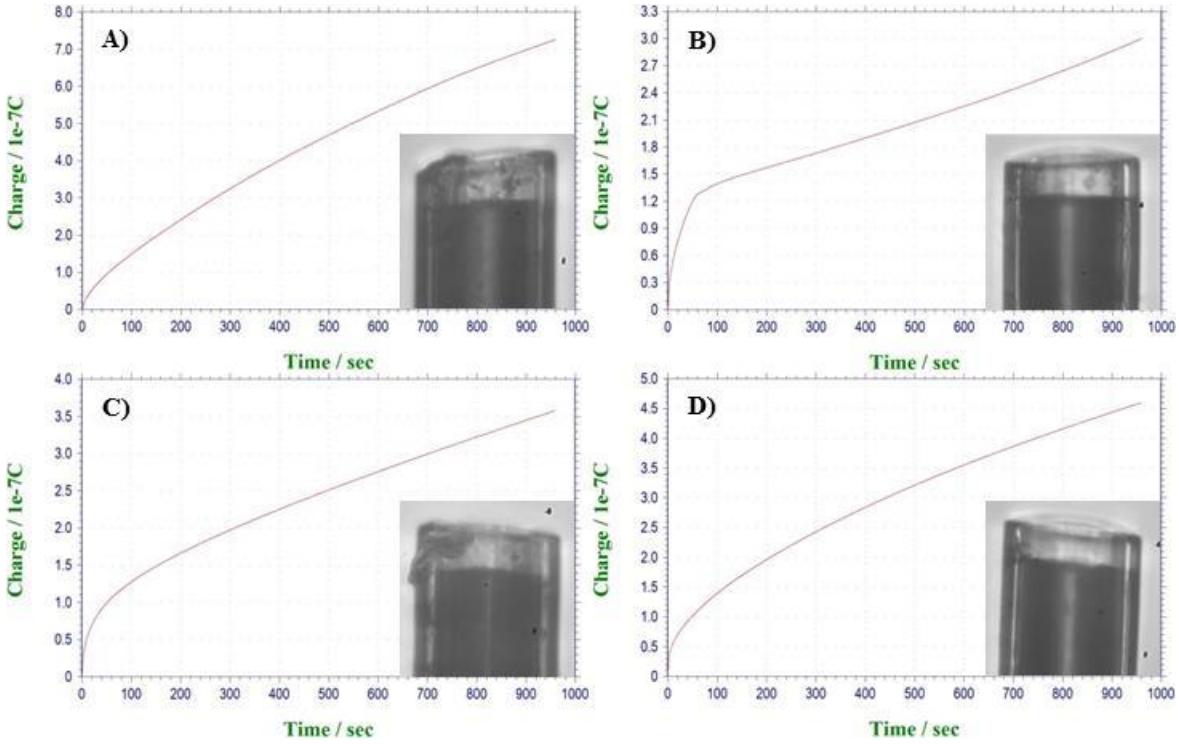

Figure 4.4 Charge vs. time curves for electrodeposition of glutarylated (A-B) and succinylated (C-D) Fe_3O_4@TEOS/APTS NPs coupled to GOx under harsh (300 µM EDC/400 µM NHS, A and C) and mild (3 µM EDC/4 µM NHS, B and D) coupling conditions.

Utilizing the Stokes-Einstein equation assuming spherical bioconjugates, one can solve for the amount of charge per particle from the ionic mobility that was measured during electrophoretic light scattering to measure the ζ potential of the particles. Rearranging Equation 3.1, the charge per glutarylated Fe_3O_4@TEOS/APTS aggregate was calculated to be 7.6 nC. Based on the deposition curves in Figure 4.4 and assuming all charge accumulation was the result of nanoparticle deposition, approximately 100 (Figure 4.4A) and 40 (Figure 4.4B) bioconjugates were deposited. Similarly, the charge per succinylated Fe_3O_4@TEOS/APTS aggregate was calculated to be 12 nC, approximating the total number of bioconjugates deposited to be 30 (Figure 4.4C) and 40 (Figure 4.4D).

Glucose Oxidase as derived from Aspergillus niger is approximately 7 x 7 x 22 nm.[35] Utilizing the longest dimension of 22 nm and the DLS-measured diameter of 212.6 nm for

glutarylated Fe_3O_4@TEOS/APTS aggregates shown in Chapter 3, the bioconjugate could be modelled as a sphere with a diameter of 256 nm, assuming an even coating of the enzyme around the nanoparticle surface. Provided a platinum electrode surface with a diameter of 25μm, a maximum of 7400 spherical bioconjugates could be deposited in a single layer at the electrode surface.[36] Based on this calculation, deposition proved inefficient by this method if close-packed layers are to be deposited, and the significant decline in current during deposition is more likely to be due to electrostatic repulsion between deposited bioconjugates and those suspended rather than the formation of a resistive layer of material on the surface. Admittedly, this estimation uses the calculated charge per succinylated or glutarylated Fe_3O_4@TEOS/APTS aggregate without enzyme attachment. The conjugation of GOx via amide bond formation would diminish the amount of surface charge and increase the number of bioconjugates deposited. The electrophoretic light scattering measurements of the bioconjugates were not examined as batches of enzyme functionalized particles were not returned to this group for study. Regardless, this estimation shows that the number of deposited bioconjugates is at least two orders of magnitude less than the close-packed maximum for a single layer and even less for a completely filled cavity that is 10 μm deep.

4.3.3. Sensor Response to Glucose

Following electrodeposition of the bioconjugates into a capillary electrode, the amperometric response to glucose was observed. Figure 4.5 presents the glucose response for two 1 mM increases in glucose for the sensors examined in Figure 4.3 and Figure 4.4. In all cases, the current increased less than 10 pA per 1 mM increase in glucose.

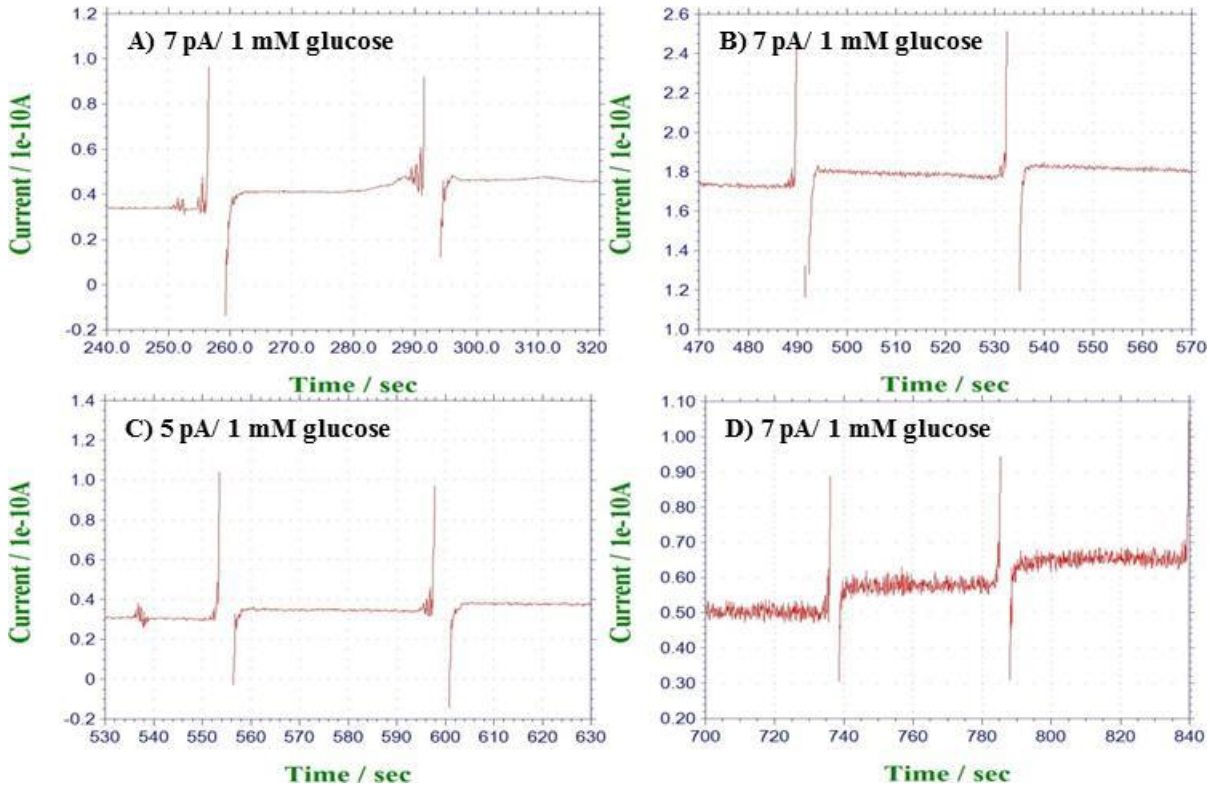

Figure 4.5 Amperometric sensor response to Δ[glucose] = 1 mM utilizing glutarylated (A-B) and succinylated (C-D) Fe_3O_4@TEOS/APTS NPs coupled to GOx under harsh (300 µM EDC/400 µM NHS, A and C) and mild (3 µM EDC/4 µM NHS, B and D) coupling conditions.

Based on electrodepositing fewer than 100 bioconjugates into the sensor cavity for both Figure 4.5A and Figure 4.5B, one can extend the hard sphere modeling approximation to calculate the expected amperometric response at saturating glucose conditions. Assuming a 212 nm aggregate and GOx attachment on its roughly 7 x 7 nm face, about 11500 enzyme molecules could be covalently attached per aggregate. With a saturating glucose concentration and an enzyme turnover number of 300 (corresponding to 600 electrons per second),[i,37] 50 deposited bioconjugates should yield a current of 55 pA. This assumes tremendous steric crowding of the

[i] The turnover number for glucose oxidase was measured by amplex red assay[33] by the Richter Research Group.

enzymes, potentially preventing enzymes from undergoing necessary conformational changes during catalysis. Additionally, thorough enzyme coverage around the Fe_3O_4@TEOS/APTS charge carrier would greatly decrease the ζ potential and negatively impact the efficiency of deposition. While simplistic, this calculation shows that picoamps of response are consistent with our deposition measurements. Given the rapid conversion of hydrogen peroxide back to molecular oxygen at the electrode surface, it is reasonable to assume a higher turnover number for the enzyme, resulting from a higher Michaelis constant for glucose as oxygen concentrations can be assumed high and constant, as discussed in the introduction to this chapter.[38] Since electron transfer turnover rates for glucose oxidase have been realized as high as ~5000 by Willner et al.,[39] achieving higher response currents with less densely packed enzyme molecules may also be feasible.

At this point, this work would require substantially more investigation into various conditions for enzyme coupling, charge-carrier diameter, and electrodeposition conditions. Assuming coulombic repulsion is disrupting deposition rather than increased resistance at the electrode surface, dextran or PEG surface coatings may be considered to provide a less densely charged particle surface to reduce the repulsive interaction. Optimizing the response in the simple buffered medium is essential prior to use in a more complex medium where background noise could be on the order of picoamps. This could be caused by the presence of other molecules for which gluxose oxidase has an affinity, such as mannose, galactose, xylose, urate, and ascorbate, where the two former electroactive species can also cause negative interference and lead to a decrease in sensitivity of a glucose sensor.[32,40] Poly(phenol) has been shown to reduce interference due to ascorbate, but likewise at the expense of glucose response.[38]

4.4. Conclusions

The provided electrode cavities were analyzed by SEM, and microscopy and elemental composition analysis revealed significantly improved electrode surfaces prior to deposition as a result of washing steps to remove residue left behind during the fabrication process. Enzyme conjugation and electrodeposition were conducted utilizing the amino-functionalized aggregates developed in Chapter 3, and a maximum of current of 7 pA was realized for 1 mM increases in glucose. Based on the charge accumulation curves and a modeling estimate using close-packed hard spheres, deposition was inefficient. The inefficiency of the deposition suggests that uniformity of nanoparticle surface functionalization requires optimization. As deposition calculations were made without ionic mobility values for particle-enzyme conjugates, future work should ensure electrophoretic light scattering data is achieved after enzyme attachment. Regardless, the experimental response is reasonable given the modeling assumptions made. Ultimately, the complexity of a biological medium *in vivo* leaves the achieved response sub-optimal and mandates further optimization.

5. Conclusions and Future Work

Synthetic control of magnetite iron oxide nanoparticles was achieved via a facile thermal decomposition method in a high boiling point solvent using a previously unreported iron (III) stearate precursor, providing a potentially more economical precursor for commercial up-scaling and reproducibility of hydrophobic Fe_3O_4 nanoparticles. By modifying initial surfactant concentrations, linear correlations between nucleation windows and resultant mean particle core diameters were observed from 8 to 16 nm by TEM, showing consistency with and providing a practical synthetic application of nucleation theory. Empirical growth modeling over varying annealing times at low surfactant concentrations yielded a grain growth exponent of ca. 22 and a precise model when compared to higher surfactant concentrations. Temperature variations should be made to further explore the validity of the model used, as well as to experimentally determine the activation energy. As was found during surface functionalization work, dynamic light scattering measurements should be made along with electron microscopy work to understand aggregation behavior in suspensions. Additionally, magnetic properties should be investigated to accompany and potentially explain DLS results.

Surface functionalization by silane condensation and cyclic anhydride ring opening to yield a carboxylated surface for enzyme attachment was non-uniform and unsuccessful. Surface carboxylation did lead to increasingly negative ζ potentials at pH 7 compared to nearly neutral amino-functionalized aggregates as expected. Despite this encouragement, DLS measurements revealed nanoparticle aggregates on the order of several hundred nanometers, and electron microscopy confirmed amorphous silica-bound aggregates of magnetite cores consistent with DLS data. This was attributed to the behavior of hydrophobic iron oxide nanoparticles prior to functionalization; as synthesized 14 nm hydrophobic particles aggregated in hexane prior to

functionalization to give aggregates from 30 nm to 1 μm in diameter. This aggregation could be the result of non-superparamagnetic iron oxide, but no measurements were made to investigate this hypothesis. Efforts in nanoparticle surface functionalization must focus on the dynamic behavior of particles in both aqueous and non-polar organic suspensions rather than relying solely on measurements made in the vacuum of an electron microscope to determine the core diameter or other dimensions for non-spherical nanostructures. Differences in ζ potentials and ultimately total charge per aggregate between succinylated and glutarylated derivatives were attributed to increased torsional strain in succinic anhydride. Further attention may be paid to this by examining the use of malonic anhydride for the generation of a carboxylated nanoparticle surface; the potential increase in the magnitude of the resultant ζ potential and surface charge could prove useful in improving colloidal stability of functionalized particles. However, derivatives from malonic anhydride may hamper deposition due to increased coulombic repulsion resulting from higher charge densities per particle or aggregate.

Bioconjugation of carboxylated magnetite nanoparticle aggregates to glucose oxidase was performed, and electrodeposition of these bioconjugates into glass/platinum capillary electrodes yielded sub-optimally functional amperometric sensors. Less than 100 bioconjugates were deposited into the cavity in each case as calculated from the total accumulated charge during electrodeposition using electrophoretic light scattering data. The maximum response current of 7 pA was of the same order of magnitude as predicted by a glucose saturated model, assuming spherical aggregates and close-packing aggregates during deposition and a sterically hindered arrangement of enzymes on a sphere's surface. The deposition of only a single or thin layer of material at the electrode could be due to the negative surface charge of the bioconjugates leading to electrostatic repulsion between conjugates, preventing further deposition and limiting

the glucose response. The sensor response protocol was limited to several 1.0 mM glucose additions, but future work should explore higher concentrations, including saturation. This would allow for a more direct comparison to modeling efforts, as well as an understanding of the linear dynamic range of the assay. The effect of spatial confinement within the capillary could be studied with a quartz crystal microbalance in hopes of negating coulombic repulsions between bioconjugates that may cause inefficient electrodeposition. Additionally, the time evolution of the amount of deposited material after the deposition potential is removed could be studied. More complex media should be explored; however, optimizations of the particle surface functionalization, enzyme conjugation protocol, and deposition method should first be considered.

6. References

1. Rodriguez, M. A.; Armstrong, D. W., Separation and analysis of colloidal/nano-particles including microorganisms by capillary electrophoresis: a fundamental review. *Journal of Chromatography B* **2004,** *800* (1), 7-25.
2. Matsumoto, N.; Chen, X.; Wilson, G. S., Fundamental studies of glucose oxidase deposition on a Pt electrode. *Analytical chemistry* **2002,** *74* (2), 362-367.
3. Pazur, J. H.; Kleppe, K., The Oxidation of Glucose and Related Compounds by Glucose Oxidase from Aspergillus niger*. *Biochemistry* **1964,** *3* (4), 578-583.
4. Khatun Haq, S.; Faiz Ahmad, M.; Hasan Khan, R., The acid-induced state of glucose oxidase exists as a compact folded intermediate. *Biochemical and biophysical research communications* **2003,** *303* (2), 685-692.
5. Imisides, M. D.; John, R.; Riley, P. J.; Wallace, G. G., The use of electropolymerization to produce new sensing surfaces: a review emphasizing electrode position of heteroaromatic compounds. *Electroanalysis* **1991,** *3* (9), 879-889.
6. Luo, X.-L.; Xu, J.-J.; Du, Y.; Chen, H.-Y., A glucose biosensor based on chitosan–glucose oxidase–gold nanoparticles biocomposite formed by one-step electrodeposition. *Analytical Biochemistry* **2004,** *334* (2), 284-289.
7. Manriquez, J.; Godínez, L. A., Tuning the structural, electrical and optical properties of Ti (III)-doped nanocrystalline TiO< sub> 2</sub> films by electrophoretic deposition time. *Thin Solid Films* **2007,** *515* (7), 3402-3413.
8. Cao, M.; Li, Z.; Wang, J.; Ge, W.; Yue, T.; Li, R.; Colvin, V. L.; Yu, W. W., Food related applications of magnetic iron oxide nanoparticles: Enzyme immobilization, Protein purification, and food analysis. *Trends in Food Science & Technology* **2012,** *27* (1), 47-56.
9. Nowicka, A. M.; Kowalczyk, A.; Jarzebinska, A.; Donten, M.; Krysinski, P.; Stojek, Z.; Augustin, E.; Mazerska, Z., Progress in targeting tumor cells by using drug-magnetic nanoparticles conjugate. *Biomacromolecules* **2013,** *14* (3), 828-833.
10. Laurent, S.; Forge, D.; Port, M.; Roch, A.; Robic, C.; Vander Elst, L.; Muller, R. N., Magnetic iron oxide nanoparticles: synthesis, stabilization, vectorization, physicochemical characterizations, and biological applications. *Chemical reviews* **2008,** *108* (6), 2064-2110.
11. Sadhukha, T.; Niu, L.; Wiedmann, T. S.; Panyam, J., Effective Elimination of Cancer Stem Cells by Magnetic Hyperthermia. *Molecular pharmaceutics* **2013,** *10* (4), 1432-1441.
12. LaMer, V. K.; Dinegar, R. H., Theory, production and mechanism of formation of monodispersed hydrosols. *Journal of the American Chemical Society* **1950,** *72* (11), 4847-4854.
13. Wang, F.; Richards, V. N.; Shields, S. P.; Buhro, W. E., Kinetics and Mechanisms of Aggregative Nanocrystal Growth. *Chemistry of Materials* **2013**.
14. Sun, S.; Zeng, H.; Robinson, D. B.; Raoux, S.; Rice, P. M.; Wang, S. X.; Li, G., Monodisperse MFe2O4 (M= Fe, Co, Mn) nanoparticles. *Journal of the American Chemical Society* **2004,** *126* (1), 273-279.
15. Casula, M. F.; Jun, Y.-w.; Zaziski, D. J.; Chan, E. M.; Corrias, A.; Alivisatos, A. P., The Concept of Delayed Nucleation in Nanocrystal Growth Demonstrated for the Case of Iron Oxide Nanodisks. *Journal of the American Chemical Society* **2006,** *128* (5), 1675-1682.
16. Jana, N. R.; Chen, Y.; Peng, X., Size-and shape-controlled magnetic (Cr, Mn, Fe, Co, Ni) oxide nanocrystals via a simple and general approach. *Chemistry of materials* **2004,** *16* (20), 3931-3935.

17. Otsu, N., A threshold selection method from gray-level histograms. *Automatica* **1975,** *11* (285-296), 23-27.
18. Qi, B.; Ye, L.; Stone, R.; Dennis, C.; Crawford, T. M.; Mefford, O. T., Influence of Ligand–Precursor Molar Ratio on the Size Evolution of Modifiable Iron Oxide Nanoparticles. *The Journal of Physical Chemistry C* **2013,** *117* (10), 5429-5435.
19. Lifshitz, I. M.; Slyozov, V. V., The kinetics of precipitation from supersaturated solid solutions. *Journal of Physics and Chemistry of Solids* **1961,** *19* (1), 35-50.
20. Yue, C.; Zhang, L.; Liao, S.; Gao, H., Kinetic analysis of the austenite grain growth in GCr15 steel. *Journal of materials engineering and performance* **2010,** *19* (1), 112-115.
21. (a) Polikov, V. S.; Tresco, P. A.; Reichert, W. M., Response of brain tissue to chronically implanted neural electrodes. *Journal of neuroscience methods* **2005,** *148* (1), 1-18; (b) Biran, R.; Martin, D. C.; Tresco, P. A., Neuronal cell loss accompanies the brain tissue response to chronically implanted silicon microelectrode arrays. *Experimental neurology* **2005,** *195* (1), 115-126.
22. Chu, B., Dynamic light scattering. *Soft Matter Characterization* **2008**, 335-372.
23. Delgado, A. V.; Gonzalez-Caballero, F.; Hunter, R.; Koopal, L.; Lyklema, J., Measurement and interpretation of electrokinetic phenomena. *Journal of colloid and interface science* **2007,** *309* (2), 194-224.
24. Gupta, A. K.; Gupta, M., Synthesis and surface engineering of iron oxide nanoparticles for biomedical applications. *Biomaterials* **2005,** *26* (18), 3995-4021.
25. Altikatoglu, M.; Basaran, Y.; Arioz, C.; Ogan, A.; Kuzu, H., Glucose oxidase-dextran conjugates with enhanced stabilities against temperature and pH. *Applied biochemistry and biotechnology* **2010,** *160* (8), 2187-2197.
26. De Palma, R.; Peeters, S.; Van Bael, M. J.; Van den Rul, H.; Bonroy, K.; Laureyn, W.; Mullens, J.; Borghs, G.; Maes, G., Silane ligand exchange to make hydrophobic superparamagnetic nanoparticles water-dispersible. *Chemistry of Materials* **2007,** *19* (7), 1821-1831.
27. (a) Sehgal, D.; Vijay, I. K., A method for the high efficiency of water-soluble carbodiimide-mediated amidation. *Analytical biochemistry* **1994,** *218* (1), 87-91; (b) Staros, J. V.; Wright, R. W.; Swingle, D. M., Enhancement by< i> N</i>-hydroxysulfosuccinimide of water-soluble carbodiimide-mediated coupling reactions. *Analytical biochemistry* **1986,** *156* (1), 220-222.
28. Hermanson, G. T., *Bioconjugate techniques*. Academic press: 1996.
29. IR Spectroscopy Tutorial: Amines. http://orgchem.colorado.edu/Spectroscopy/irtutor/aminesir.html (accessed May 19, 2014).
30. Eberson, L.; Landström, L., Studies on cyclic anhydrides. *Acta Chemica Scandinavica* **1972,** *26*, 239-249.
31. Ault, A., An introduction to enzyme kinetics. *Journal of Chemical Education* **1974,** *51* (6), 381.
32. Gibson, Q. H.; Swoboda, B. E.; Massey, V., Kinetics and mechanism of action of glucose oxidase. *Journal of Biological Chemistry* **1964,** *239* (11), 3927-3934.
33. Harris, D. C., *Exploring chemical analysis*. Macmillan: 2012.
34. Petillo, P. A.; Wilson, G. S.; Wu, J. Z.; Richter, M. L.; Johnson, D. A.; Aillon, D. V. Tissue implantable microbiosensor. December 5, 2013, December 5, 2013.
35. (a) Wohlfahrt, G.; Witt, S.; Hendle, J.; Schomburg, D.; Kalisz, H. M.; Hecht, H.-J., 1.8 and 1.9 A resolution structures of the Penicillium amagasakiense and Aspergillus niger glucose

oxidases as a basis for modelling substrate complexes. *Acta Crystallographica Section D: Biological Crystallography* **1999,** *55* (5), 969-977; (b) Seehuber, A.; Dahint, R., Conformation and Activity of Glucose Oxidase on Homogeneously Coated and Nanostructured Surfaces. *The Journal of Physical Chemistry B* **2013,** *117* (23), 6980-6989.
36. Smaller Circles in a Larger Circle. http://www.engineeringtoolbox.com/smaller-circles-in-larger-circle-d_1849.html (accessed May 15, 2014).
37. Zhou, M.; Diwu, Z.; Panchuk-Voloshina, N.; Haugland, R. P., A stable nonfluorescent derivative of resorufin for the fluorometric determination of trace hydrogen peroxide: applications in detecting the activity of phagocyte NADPH oxidase and other oxidases. *Analytical biochemistry* **1997,** *253* (2), 162-168.
38. Bartlett, P. N.; Caruana, D. J., Electrochemical immobilization of enzymes. Part V. Microelectrodes for the detection of glucose based on glucose oxidase immobilized in a poly (phenol) film. *Analyst* **1992,** *117* (8), 1287-1292.
39. Xiao, Y.; Patolsky, F.; Katz, E.; Hainfeld, J. F.; Willner, I., " Plugging into enzymes": nanowiring of redox enzymes by a gold nanoparticle. *Science* **2003,** *299* (5614), 1877-1881.
40. Lowry, J. P.; McAteer, K.; El Atrash, S. S.; Duff, A.; O'Neill, R. D., Characterization of glucose oxidase-modified poly (phenylenediamine)-coated electrodes in vitro and in vivo: homogeneous interference by ascorbic acid in hydrogen peroxide detection. *Analytical Chemistry* **1994,** *66* (10), 1754-1761.